

AWARD NUMBER: W81XWH-16-1-0018

TITLE: A 3D Bioprinted Model for the Study of Premalignant Breast Disease

PRINCIPAL INVESTIGATOR: Adam W. Feinberg, PhD

CONTRACTING ORGANIZATION: Carnegie Mellon University
Pittsburgh, PA 15213

REPORT DATE: May 2017

TYPE OF REPORT: Annual

PREPARED FOR: U.S. Army Medical Research and Materiel Command
Fort Detrick, Maryland 21702-5012

DISTRIBUTION STATEMENT: Approved for Public Release;
Distribution Unlimited

The views, opinions and/or findings contained in this report are those of the author(s) and should not be construed as an official Department of the Army position, policy or decision unless so designated by other documentation.

REPORT DOCUMENTATION PAGE				Form Approved OMB No. 0704-0188	
Public reporting burden for this collection of information is estimated to average 1 hour per response, including the time for reviewing instructions, searching existing data sources, gathering and maintaining the data needed, and completing and reviewing this collection of information. Send comments regarding this burden estimate or any other aspect of this collection of information, including suggestions for reducing this burden to Department of Defense, Washington Headquarters Services, Directorate for Information Operations and Reports (0704-0188), 1215 Jefferson Davis Highway, Suite 1204, Arlington, VA 22202-4302. Respondents should be aware that notwithstanding any other provision of law, no person shall be subject to any penalty for failing to comply with a collection of information if it does not display a currently valid OMB control number. PLEASE DO NOT RETURN YOUR FORM TO THE ABOVE ADDRESS.					
1. REPORT DATE May 2017		2. REPORT TYPE Annual		3. DATES COVERED 1 May 2016 - 30 Apr 2017	
4. TITLE AND SUBTITLE A 3D Bioprinted Model for the Study of Premalignant Breast Disease				5a. CONTRACT NUMBER	
				5b. GRANT NUMBER W81XWH-16-1-0018	
				5c. PROGRAM ELEMENT NUMBER	
6. AUTHOR(S) Adam W. Feinberg, PhD feinberg@andrew.cmu.edu				5d. PROJECT NUMBER	
				5e. TASK NUMBER	
				5f. WORK UNIT NUMBER	
7. PERFORMING ORGANIZATION NAME(S) AND ADDRESS(ES) Carnegie Mellon University 5000 Forbes Ave, Pittsburgh, PA 15213				8. PERFORMING ORGANIZATION REPORT NUMBER	
9. SPONSORING / MONITORING AGENCY NAME(S) AND ADDRESS(ES) U.S. Army Medical Research and Materiel Command Fort Detrick, Maryland 21702-5012				10. SPONSOR/MONITOR'S ACRONYM(S)	
				11. SPONSOR/MONITOR'S REPORT NUMBER(S)	
12. DISTRIBUTION / AVAILABILITY STATEMENT Approved for Public Release; Distribution Unlimited					
13. SUPPLEMENTARY NOTES					
14. ABSTRACT This proposal involves a multidisciplinary team including a surgical oncologist, a mammary gland biologist, a biomedical engineer, and a cancer biologist. We hypothesize that a novel in vitro 3D bioprinted model of premalignant breast cells growing within a breast ductal system will represent the first and most faithful representation of premalignant progression in vitro and will be an outstanding model for identify markers of low-risk premalignant disease which doesn't require treatment. In the first year of the proposal we have comprehensively quantified mammary gland development in multiple different mouse strains, finding strain dependent differences highlighting a genetic component to the development. We have imaged these glands and performed proof-of-principle 3D printing. We have printed simple ductal structures (tubes) and seeded breast epithelial cells. The next year we will continue to develop and characterize the 3D model system.					
15. SUBJECT TERMS None listed					
16. SECURITY CLASSIFICATION OF:			17. LIMITATION OF ABSTRACT	18. NUMBER OF PAGES	19a. NAME OF RESPONSIBLE PERSON
a. REPORT	b. ABSTRACT	c. THIS PAGE			USAMRMC
Unclassified	Unclassified	Unclassified	Unclassified	25	19b. TELEPHONE NUMBER (include area code)

Table of Contents

1) Introduction.....	3
2) Keywords.....	3
3) Accomplishments.....	3
4) Impact.....	24
5) Changes/problems.....	24
6) Products.....	25
7) Participants and other collaborating organizations.....	25
8) Special reporting requirements.....	25
9) Appendices.....	25

1) Introduction

This proposal involves a multidisciplinary team including a surgical oncologist, a mammary gland biologist, a biomedical engineer, and a cancer biologist. **We hypothesize that a novel in vitro 3D bioprinted model of premalignant breast cells growing within a breast ductal system will represent the first and most faithful representation of premalignant progression *in vitro* and will be an outstanding model for identify markers of low-risk premalignant disease which doesn't require treatment.** In the first year of the proposal we have comprehensively quantified mammary gland development in multiple different mouse strains, finding strain dependent differences highlighting a genetic component to the development. We have imaged these glands and performed proof-of-principle 3D printing. We have printed simple ductal structures (tubes) and seeded breast epithelial cells. The next year we will continue to develop and characterize the 3D model system.

2) Keywords

DCIS, ductal cancer in situ, 3D bioprinting

3) Accomplishments

Regulatory approvals (University of Pittsburgh)

- a) Obtained IRB approval at Pitt and IACUC approval at BCM for studies
- b) Received HRPO/ACURO approval

Regulatory approvals (Carnegie Mellon University)

- a) Obtained IRB letter of exemption that the work is not human subjects research.

Research progress

Major Task 1 had 6 subtasks outlined for completion during year 1. This work was primarily focused at the University of Pittsburgh under the leadership of Patnering PI Adrian Lee. Although not all of these have been completed to date, the first three are either completed or on track to be completed soon.

Major Task 2 had 4 subtasks outlined for completion during year 1, and 2 subtasks to be initiated during year 1 and extending into year 2. This work was primarily focused a Carnegie Mellon University under the leadership of partnering PI Adam Feinberg. Although not all of these have been completed to date, 3 subtasks are completed and the rest are on track to be completed soon.

Task 1 Subtask 1 was to be completed during months 2 through 6 and was to purchase and breed mating pairs for 12 strains of mice from which to isolate mammary tissue wholemounts for 3D imaging from virgin females at 2 developmental ages. Funds to execute the studies were received on June 24th 2016. At this point we initiated the purchasing of breeding pairs for each of the strains. All twelve strain were received into our animal facility by the end of January 2017. Of these we have been able to establish productive breeding colonies for 11. One of the 12 strains, CAST/EiJ, has been difficult to obtain offspring from in high enough numbers to be useful despite the fact that we purchased additional mating pairs to compensate for reduced fecundity in this strain.

Task 1 Subtask 2 was to be completed during months 4-8 and consisted of whole mounting mammary glands (60) from post-natal day 17 (PN17) mice, stain with luminal and myoepithelial markers, and capture tomography data at the OIVM core. This age of mouse was chosen because it represents an age just prior to the onset of puberty where there is development of the gland, but this development is relatively simple and not yet under the dominating influence of estrus cycles. This subtask is still in progress. Of the 12 strains that were targeted for analysis at PN17, 7 have been completed and the remaining 5 are ongoing. Examples of a dual stained samples highlights the organization of the ductal tree and surrounding vasculature in a PN17 mammary whole mount prepared from KK/HIJ (Fig 1A). Examples of dual labeling in post-pubertal mice (B), and human mammary biopsy samples (C) is also shown and will be discussed in more detail below.

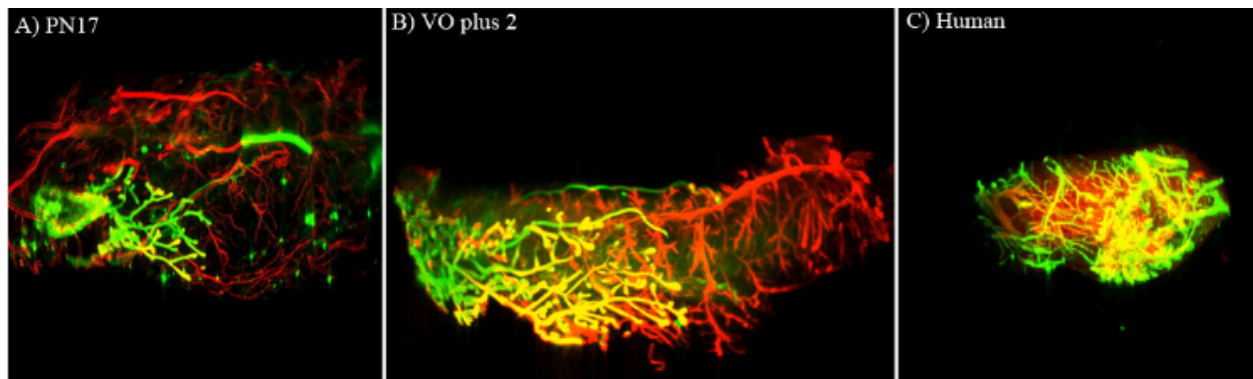


Figure 1. 3D reconstructions of Mouse and Human Mammary tissue. Mammary glands are shown from mice at post-natal day 17 (A) and 2 weeks post-vaginal opening (PN64) (B), and from a biopsy sample of normal human breast (C). Staining for E-cadherin (green) highlights the ductal epithelium. Staining for alpha-smooth muscle actin highlights blood vessels (red) and ductal myoepithelial cell layer (yellow).

Task 1 Subtask 3 was to be completed during months 4-8 and consisted of segmentation, annotation, and measurement of the ductal trees in 3D reconstructions obtained in Subtask 2. This subtask is still in progress. To date, 5 of the 12 strains that were planned have been completed and data from the remaining 7 strains is being processed as they are collected under subtask 2. All of the PN17 reconstruction data from the 5 completed strains has also been sent to the University of Pittsburg for 3D printing. A summary of the data from the 5 completed strains was also presented in a poster on April 25th at the 2017 Experimental Biology Meetings in Chicago IL. This work represents the first 3D comparison of ductal architecture and patterning in inbred mouse strains of different genetic backgrounds. The hypothesis for the study was that ductal patterning, and the implementation of stereotypical branching behaviors during early post-natal development differs with genetic background. The TreeSurveyor (Short and coworkers, 2013) software package was used to identify and annotate all of the ductal segments and branchpoints in each reconstructed tree (Figure 2). Once identified the TreeSurveyor Package then measures the geometry of these ductal features and generates a report which can then be used for summary and comparison among samples and among strains. The measurements collected on each sample included; generation number, total branch count, branches per generation, segment diameter, segment length, segment curvature, and segment, volume. For

each segment both parental and progeny segments were identified and the bifurcation and dihedral angles at each branch point are measured. Geometric endpoints are then analyzed both on a global level and on a per generation level to test for regional variations. The TreeSurveyor package also generates a dendrogram for each ductal tree which is then used to compare patterning within and among strains. Dendrogram patterning was compared within and among strains by calculating a discordance and inclusion metric for each dendrogram in comparison with every dendrogram within a given strain.

Comparisons among the 5 completed strains revealed that even in the genetic backgrounds studied so far, there are significant ($P < 0.05$) difference in ductal geometry and patterning. These differences were evident in ductal segment length (Figure 3A), diameter (Figure 3B), and curvature (Figure 3C), as well as in total length of the mammary ductal tree (Figure 3A, inset). With regard to ductal segment length, a comparison across branch

generation revealed the root (generation 0) was by far the longest ductal segment regardless of strains and averaged 1.3 ± 0.3 mm in KK/HIJ and 0.9 ± 0.2 mm in CZECHKK/EiJ. Interestingly enough, overall the CZECHII/EiJ strain was similar in total duct length to KK/HIJ (Figure 3A inset), while BUB/BnJ, C57BL/6J and PWK/PhJ were all considerably smaller ($P = 0.007$) than KK/HIJ. The KK/HIJ strain also exhibited a higher ($P = 0.004$) ductal diameter throughout the ductal tree. For all strains, ductal diameter was highest in the root and first generation branches and decreased with branch generation. The BUB/BnJ strain displayed the lowest overall branch diameter (Figure 3B inset). With regard to branch curvature BUB/BnJ was the highest ($P = 0.01$), while PWK/PhJ was lowest. These results support the preliminary conclusion that genetic background, presumably acting through sequence variants at specific genomic loci, is influencing ductal diameter, length, and curvature in these inbred strains. Additional traits discussed below did not show the same degree of strain-dependent variation.

Comparison of branch counts, bifurcation angles, and dihedral angles among the 5 strains completed to date is shown in Figures 4 A, B and C, respectively. With regard to branch counts although BUB/BnJ tended to have the highest and PWK/PhJ the lowest overall branch count (Figure 4A inset), considerable intra-strain variability was observed and no statistically

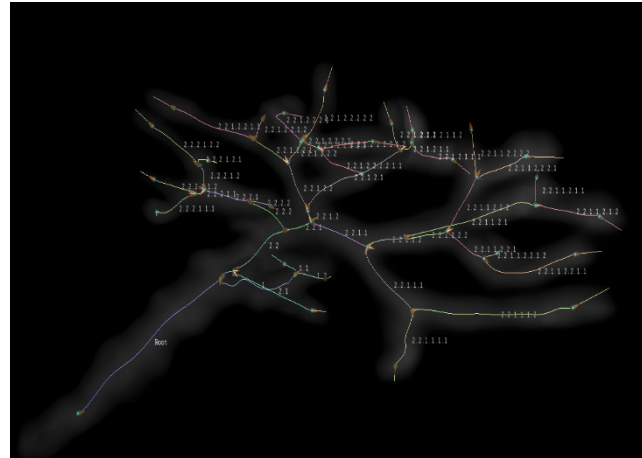


Figure 2. Annotated PN17 mammary ductal tree. Each sample is imaged in the optical projection tomograph generating 1200 digital images covering a 360° rotation. The resulting images are then reconstructed into a volume using the NRecon Software package. The ductal trees within each volume are segmented away from non-ductal components and noise using the Analyze 12.0 software package. These segmented ductal trees are then imported into the TreeSurveyor Software which identifies each of the ductal segments and branchpoints within the tree and then subsequently measures their geometric attributes.

significant differences detected. When analyzed as a function of branch generation (Figure 4A) however, there does appear to be a strain by generation interaction involving CZECHII/EiJ versus the rest of the strains. In this regard, during early branch generations the CZECHII/EiJ strain does not show the same rate of increase as the other strains. This could potentially be explained by the fact that this strain displays a lot of budding from the root of the ductal tree and each budding event, though not giving rise to a major branch, is counted as a terminal branch nonetheless. We are currently exploring other analytical approaches to account for the unique behavior in this strain.

The last traits to be measured in TreeSurveyor, were bifurcation angle (Figure 4B) and dihedral angle (Figure 4C). When analyze over the entire ductal tree, neither of these two traits displayed significant variation among strains. In addition, there did not appear to be any systematic trends in the values of these angles as a function of branch generation.

For the average bifurcation angle, the individual strain means ranged from a low of $91.4 \pm 2.9^\circ$ in C57BL/6J to a high of $99.6 \pm 1.8^\circ$ in CZECHII/EiJ (Figure 4 B inset). Although this result suggests that most bifurcation events within the PN17 mammary ductal tree occur as right angles, a closer inspection of the line graph for this trait (Figure 4B) suggests that differences among strains are apparent in the angle of very first bifurcation event that occurs at the ductal root (generation = 0). An analysis of variance that includes all to the strains displayed only borderline significance ($P=0.08$). However, just doing simple pairwise t-tests among the different strains revealed a highly significant

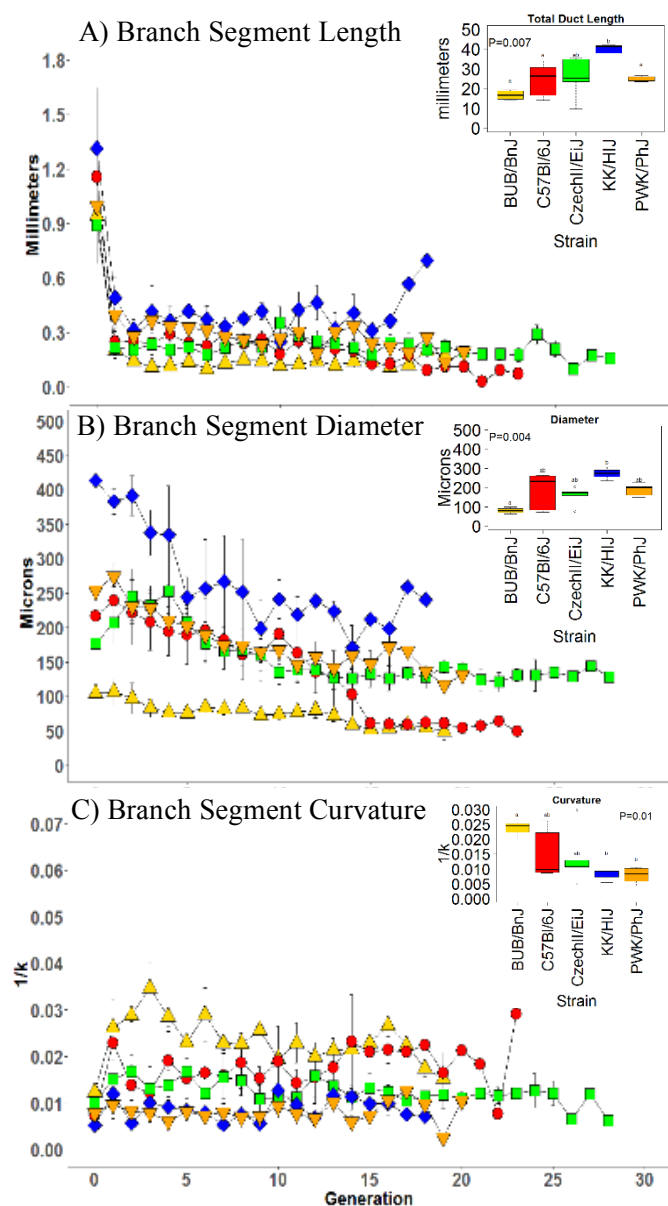


Figure 3. Comparison of mammary ductal geometry reveals differences among inbred mouse strains. Shown are branch segment length (A), total ductal tree length (A inset), branch segment diameter (B), average branch diameter over the whole tree (B inset), branch segment curvature (C), and average branch curvature over the whole tree (C inset). Each symbol represents the mean \pm s.e.m. for 3 to 6 animals. Statistical significance was set at $\alpha=0.05$.

($P=0.004$) difference between KK/HIJ and BUB/BnJ. It may be that a low sample size in the KK/HIJ samples ($N=3$) coupled with higher variability in the PWK/PhJ strain prevented detection of the effect in this preliminary ANOVA. As the sample size increases this difference could very well reach significance highlighting a patterning event that is uniquely regulated by genetic background.

For Dihedral angle (Figure 4C inset), the overall average ranged from a low of $72.3 \pm 2.9^\circ$ in BUB/BnJ to a high of $82.7 \pm 4.8^\circ$ in KK/HIJ. This result supports the suggestion that most bifurcation events occur at oblique dihedral angles that are much closer to being orthogonal than planar. Although a closer examination of dihedral angle as a function of branch generation (Figure 4C) shows an apparent difference between C57BL/6J and KK/HIJ at generation 17, we believe this is more due to an artifact of sample size rather than a real difference. Not all animals within a given strain have the same number of branch generations. Therefore as the average ductal tree for a given strain progresses from root to tip a threshold generation is reached and samples drop out. Both C57BL/6J and KK/HIJ only have a single sample for generation 17 and all subsequent generations. Although there may be several possible solutions to deal with this artifact, probably the simplest approach will be to truncate the average ductal trees for each strain to only those generations for which all individuals within the strain are present. This would at least give a true representation of each strain out to the generation for which there is adequate sampling. As the remainder of the samples are collected this approach will be tested.

The last set of traits to be compared among these PN17 samples were metrics describing the degree of conservation between the ductal structures within any given strain. For this final

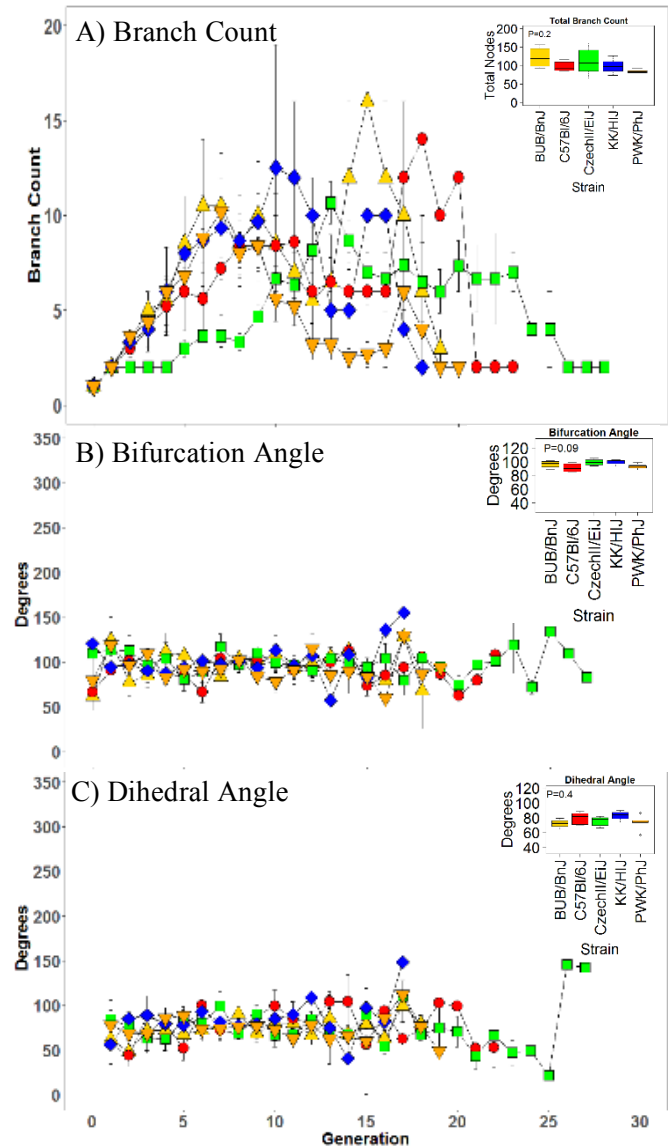


Figure 4. Comparison of branch counts and angles at PN17. Shown are branch counts (A), bifurcation angles (B), and dihedral angles (C) plotted as a function of branch generation in the 5 inbred strains that have been completed at PN17. Each symbol represents the mean \pm s.e.m. for 3 to 6 animals. Statistical significance was set at $\alpha=0.05$.

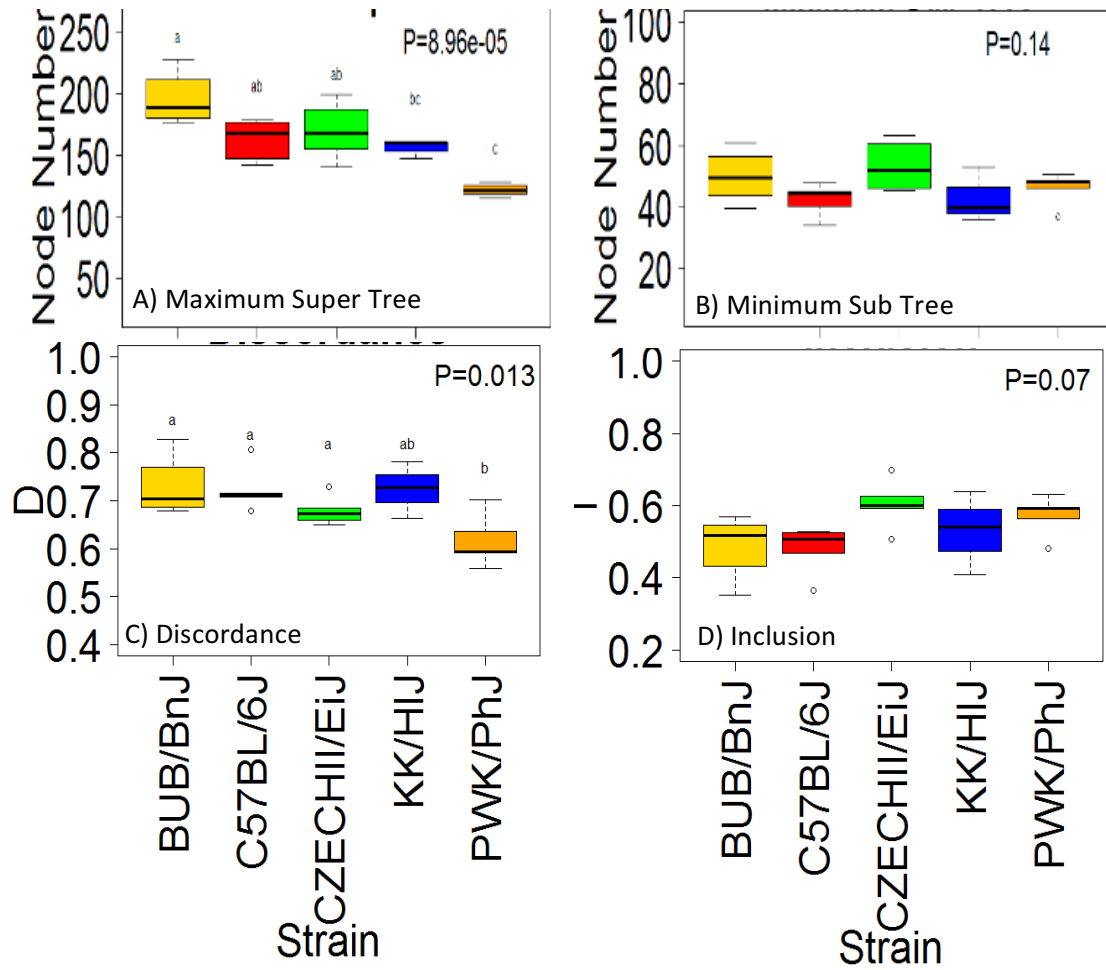


Figure 5. Comparison of Stereotypy in PN17 ductal trees from 5 strains of inbred mice. Dendrograms were generated from the 3 to 5 mice within each of the 5 strains and the used in pairwise comparisons to calculate the maximum super tree (A), minimum sub tree (B), discordance (C) and inclusion (D). Each boxplot represents the data from 3 to 6 mice. Boxes with diffing superscripts differ ($P < 0.05$).

analysis, dendrograms were aligned using a MatLab algorithm described by Lamberton and Coworkers (2015). This allows for the calculation of 4 descriptive metrics for each pairwise comparison among the individuals within a given strain. The maximum supertree (S^+) is given by the number of nodes present in the union of a given pair of dendrograms (Figure 5A). The minimum subtree (S^-) is represent by the number of nodes present in the intersection of a given pair of dendrograms (Figure 5B). From these two metrics, a difference, or discordance, metric (Figure 5C) is calculated as $D = (|S^+ - S^-|) / |S^+|$. A final metric referred to as Inclusion (Figure 5D) is calculated as $I = |S^-| / (\min T_1, T_2)$ where T_1 and T_2 are the node counts for the two dendrograms being compared. Genetic background had significant ($P < 0.05$) effects on both the maximum supertree size and on discordance. Both of these metrics were highest in the BUB/BnJ strain and lowest in PWK/PhJ. These results support the conclusion that the implementation of stereotypy in the PN17mammary ductal tree, although relatively low, is dependent on genetic background. For a comparative perspective, prior data published on the developing fetal kidney in mice

estimates discordance at ~ 0.2 and inclusion at >0.8 . This supports the conclusion that mammary ductal pattern has a very low degree of conservation. It is important to note here, that with the current analysis we have only sampled a fraction of the known genetic variability within the mouse. This means that completion of the analysis in the remaining 7 strains is still of paramount importance to fully testing our hypothesis and establishing the extremes not only for these traits, but also for the traits to be measured on PN64 mice under Subtask 4.

Task 1 Subtask 4 was to be completed during months 6 – 9 and involved whole mount staining mammary glands (60) from PN64 mice for the same luminal and myoepithelial markers used on the PN17 mice. The data from these wholemounts was to be generated with help from the SANTA at the University of Washington. Although we continue to work on this subtask, our progress has been delayed for two reasons. Firstly, technical difficulty was encountered in processing the 3D reconstructions obtained from the SANTA facility. This difficulty arose from the fact that there were limitations in the wavelengths at which the SANTA instrumentation could image and these were incompatible with the staining protocols that were worked out in our lab. When the wholemounts were stained with dyes that were optimal for the SANTA instrumentation, although collection of imaging data was possible this data was so noisy that it was impractical to segment the ductal trees for subsequent analysis. A second reason stemmed from the fact that with limited resources to support a larger breeding colony and the personnel to carry the studies we felt that it was most efficacious to complete the PN17 data prior to moving on to a full focus on the PN64 animals. Since this decision was made we have made refinements to our procedures which we believe will produce reconstructions that can be processed and we are turning our focus more towards completion of the PN64 samples. The image in Figure 1 B is an example of a PN64 wholemount from a PWK/PhJ and illustrates that we are likely to have success with these larger samples.

Task 1 Subtask 5: Was to be completed during months 8-9 was to purchase lactating dams with litters for each of 3 rat strains. This subtask has not been started yet since we felt that it would be far better to complete the mouse analysis prior to beginning to work on the larger and challenging rat samples. That said, we have purchased staining reagents and attempted several pilot studies at using a silver-based enzyme metallography to produce wholemounts that are suitable for imaging in the Micro-CT instrument that we have at Baylor College of Medicine. Further efforts will be made on this subtask

Task 1 subtask 6: Is to be completed over the course of the next several months and consists of whole mount staining mammary glands (15) from PN64 rats, stain with luminal and myoepithelial markers, and capture tomography and Micro-CT data at the OIVM core. As describe above under subtask 5 this subtask will be completed during the coming year.

Task 2 Subtask 1 was to be completed during months 4 through 12 and was to 3D print mammary ductal structure images using ECM hydrogels. This subtask has been completed and we have fully developed and implemented this capability. To do this we needed to implement a new 3D bioprinting approach that allowed us to directly print with collagen type I and additional ECM protein hydrogels while achieving high fidelity and resolution better than 100 μm .

First, we needed to develop a process to print multiple materials, in order to have a temporary support material that would provide mechanical strength and enable handling of the delicate mammary ductal structures, which consist of small diameter tubes that branch in 3D space. A collagen hydrogel containing cells will often compact over time due to the adhesion, proliferation, and remodeling of the cells. If this process is unregulated, many constructs will compact to a dense state containing a necrotic core. Many engineered tissues consist of a cellular gel that is compacted around a mandrel or series of rigid posts meant to align internal cells based on the stresses inside the gel. In an unconstrained tubular construct, compaction would manifest as initial closure of the internal lumen and eventual fusion into a dense mass. It is therefore reasonable to expect an engineered branching construct such as a ductal epithelium to compact into a denser, dysfunctional state with necrotic regions and partial lumen closure. While it may be possible to formulate a collagenous, cellular hydrogel ink that does not compact in culture, the requirements for this are likely beyond the scope of this project. Instead, it should be easier to embed the collagen construct inside a sparse net of rigid alginate hydrogel extrusions (Figure 6A). Forces that normally deform the collagen hydrogel would instead be forced to work against the alginate mesh that surrounds the construct. The alginate would be included in the print as a separate ink in an additional extruder, and the mesh would be generated as a sparse infill pattern normally seen in the interior of 3D prints. Testing this approach of immobilizing one printed material within another would likely require a simplified geometry such as a vertical tube of collagen gel to be printed in alginate mesh (Figure 6C). Measuring the dimensions of the tube is accomplished as with the gauging of print accuracy using calibration prints – micrographs are compared with known digital dimensions. By using this approach, we can fabricate a cellular collagenous tube coated in epithelium and maintain its geometry while in culture, making it possible to then create a complete epithelial tree.

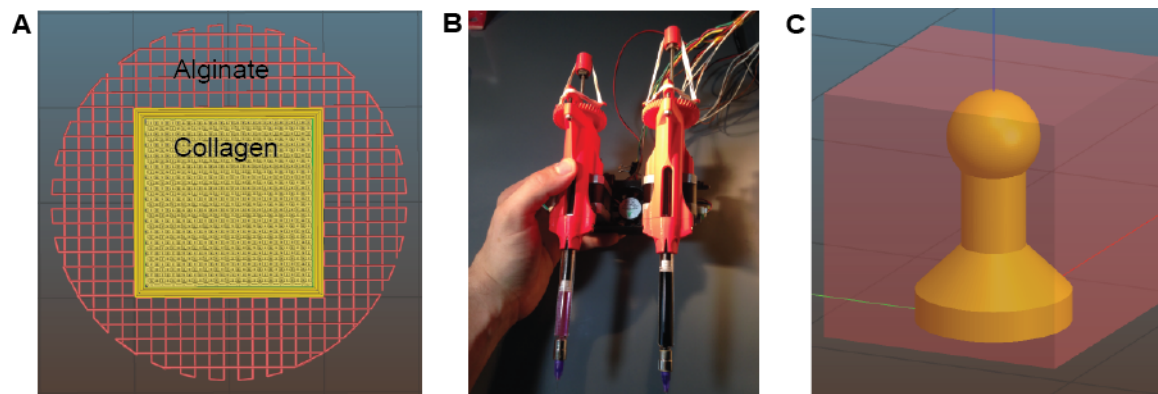


Figure 6. Utilizing Dual Extrusion to Reinforce Soft Hydrogels with Rigid Hydrogel Mesh. (A) A soft collagen hydrogel mass is 3D printed alongside a sparse net of a more rigid alginate hydrogel. (B) Two steppers power a pair of syringe pump extruders with collagen and alginate hydrogel inks. (C) A hollow tube is printed from a soft hydrogel inside an alginate mesh to preserve its shape during handling or culture.

Most unmodified collagen hydrogel 3D prints cannot be lifted out of solution without introducing permanent deformation, and this is because the collagen hydrogel is too weak to support itself outside of solution. It was thought that including a rigid hydrogel such as alginate

alongside the collagen would provide a reinforcement that would fuse to and sustain the collagen's geometry out of solution. A ring of printed collagen hydrogel supported by a printed alginate mesh shown in Figure 7A was shown to not only remained fused at the border of the two hydrogels but also maintain correct dimensions even after being transported in air multiple times. The largest dimensional deviation from the file was found at the sides of the alginate mesh, which were supposed to be 8 mm but turned out closer to 8.25 mm. The collagen ring was supposed to have an internal diameter of 4.4 mm and an outer diameter of 6 mm. In Figure 7B, the measurements for the edge of the alginate mesh, and the internal and external diameters of the collagen ring are shown. In another example, collagen sections which were manually plucked from their alginate mesh counterparts shown in Figure 7C brought with them portions of alginate mesh during dissection, as seen in Figure 7D. The fusion between the alginate and collagen portions of these multi-material prints is thought to be responsible for maintaining collagen geometry during handling. Furthermore, a multi-material collagen and alginate print of a scaled-up developing mammary duct survived a drop to the lab floor (Figure 7E). After it was recovered and imaged, it was shown to be intact and encased in alginate fibers clearly visible in Figure 7F. Further investigation into the maintenance of collagen geometry under handling forces is needed and will likely include material testing of multi-material prints. Since collagen by itself is a fragile material incapable of being delicately printed in a manner that bears its weight outside of solution, this method of reinforcing collagen with alginate presents a promising solution for creating and allowing the manipulation of complex collagen components. What's more, the collagen can be isolated from the alginate without damage by submersion in a calcium chelating bath, which results in dissolution of the alginate mesh and complete release of the collagen component, as shown in Figure 6G. Due to the presence of the alginate mesh, it is noted that these constructs could be easily handled, seeded, cultured, and fixed without every touching or interfering with the collagen component.

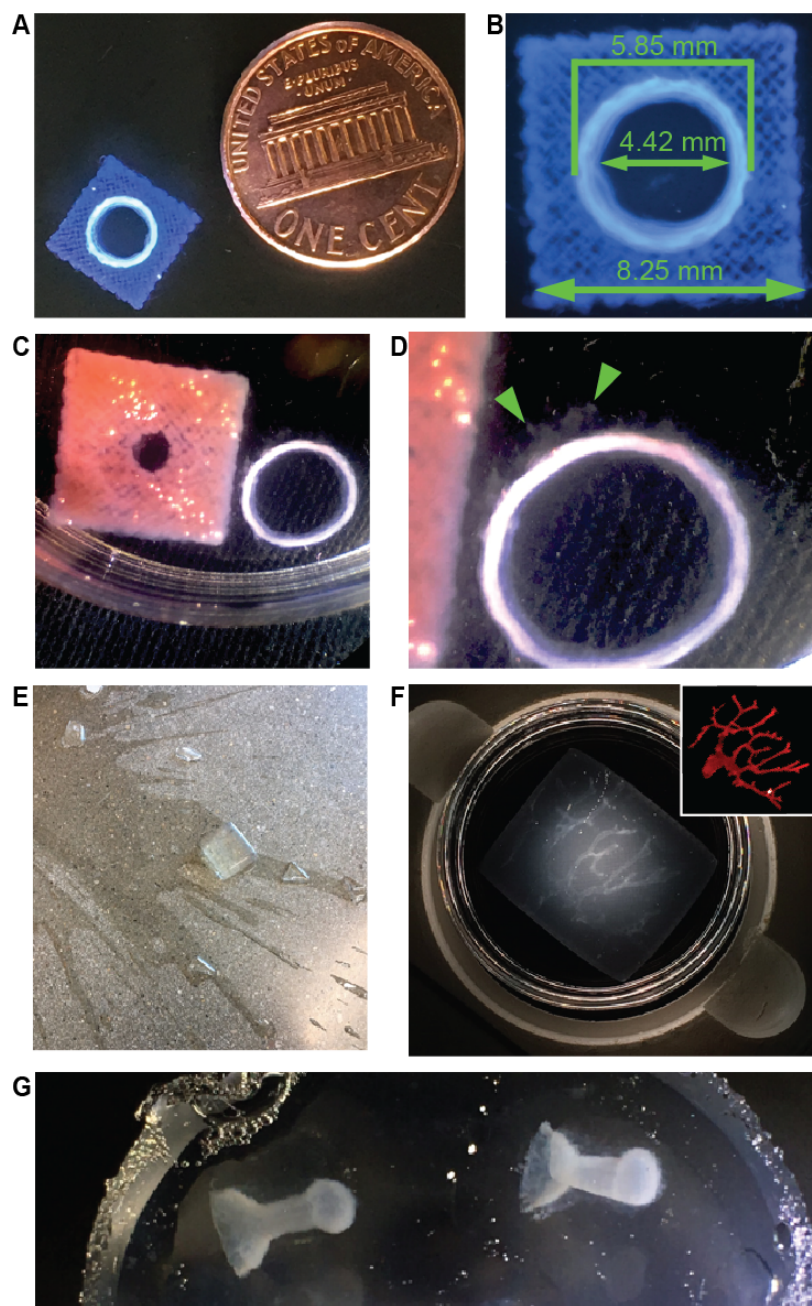


Figure 7. Stiff hydrogel components protect fragile hydrogel components in multi-material prints. (A) A multi-material print showing an inner ring of collagen hydrogel surrounded by alginate hydrogel stained with Alcian Blue. U.S. penny for scale. (B) The measured construct shows dimensions consistent with the intended diameters. (C) A dissected multi-material print showing collagen ring on right and alginate mesh on left in pink (D) The removed collagen ring shows alginate fibers that were fused to the collagen and could not be separated, proving fusion of the gels. (E) A multi-material print is shown on the floor of a lab after having fallen several feet along with shards of its parent beaker. (F) The print in (E) recovered and under dark field illumination, showing maintenance of the fragile collagen component inside the print's interior.

Inset is the file for the collagen component. **(G)** Collagen-based 3D printed tissues removed from alginate threads.

Second, replicating the in vivo environment in vitro means engineering constructs to closely mimic the appearance of in vivo equivalents. The microscopic geometry of tissues is often more complex and dynamic than we can hope to recreate with any current technology, but macroscopic features are easily replicable using 3D printing. We can process imaging data (Figure 8A) from optical projection tomography (OPT) of whole-mount tissue samples, and, through software analysis, model the tissue as a 3D printable solid (Figure 8B). By printing an entire ductal epithelium modeled from imaging data, we can ensure that the internal features of the epithelium such as the bifurcations within the branching tree are geometrically representative of native tissues (Figure 8C). Furthermore, we can change our printed epithelium to a different model derived from a different set of imaging data or parametrically alter it to suit our needs.

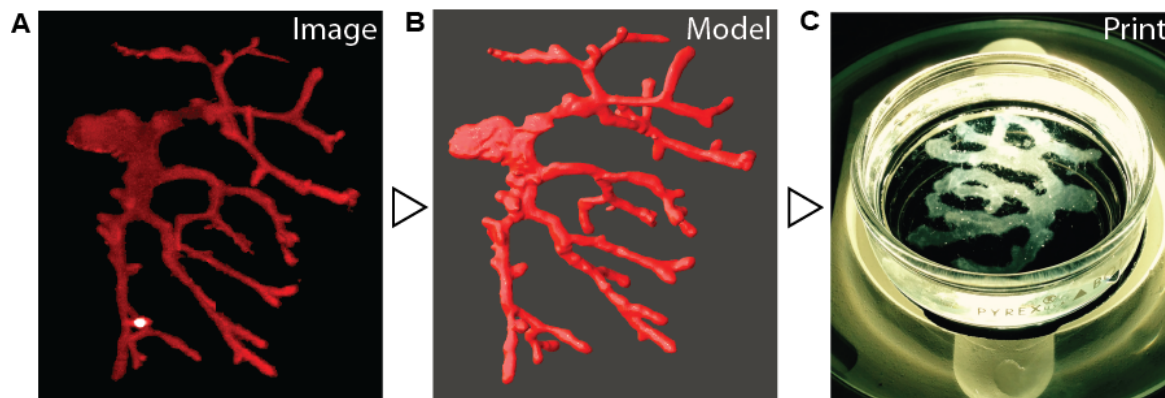


Figure 8. Imaging, modeling, and 3D printing a ductal epithelial tree. (A) A ductal epithelium tree is imaged using OPT or some other 3D scanning method. **(B)** A model of the ductal epithelium is generated from the imaging data. **(C)** A solid representation of the external geometry of the model is FRESH printed from a hydrogel shown in darkfield illumination.

Since it has been found that ductal epithelium possesses 4 distinct developmental morphologies, which are intimately associated with the 3 most commonly used mouse strains in breast cancer research, it is important to be able to vary the chosen geometry of the epithelium and obtain similar levels of accuracy across different morphologies. Verifying said accuracy of the 3D prints involves imaging them using a technique such as OPT or confocal microscopy, for the data obtained from such processes can be used to directly compare the output of the 3D printer with the input file's dimensions. We start by tackling conversion of complex image data stacks of epithelial tissues into 3D meshes that can be processed and 3D printed at numerous sizes and shapes. Next, we draw from these structures a fundamental morphology and parametrically incorporate it into a representative parametric “module” designed in CAD. This module can be edited to account for any design shortcomings while still reflecting the necessary aspects of in vivo complexity.

Task 2 Subtask 2 was to be completed during months 6-12 and consisted of tomography imaging and evaluation of 3D printed mammary ductal structure, with one sample to be

evaluated. We have made significant progress on this goal, and have completed it per the initial target milestones. However, we are still working to further improve the imaging capability and to image the 3D printed mammary duct on the same OPT system used to collect the original whole mount image of the breast mammary duct from the mouse. We 3D printed a 200% scale ductal trees from collagen type I. The files used to generate these trees were obtained from Co-investigator Dr. Hadsell and processed through several iterations of workflow that eventually resulted in a continuous, manifold mesh without visible tiling artifacts, stacking artifacts, or floating solids shown below in Figure 9A. The file was scaled to 200% to allow the printer to deposit a significant portion of the construct using a filamentous extrusion shown in the Gcode in Figure 9B rather than as punctate depositions.

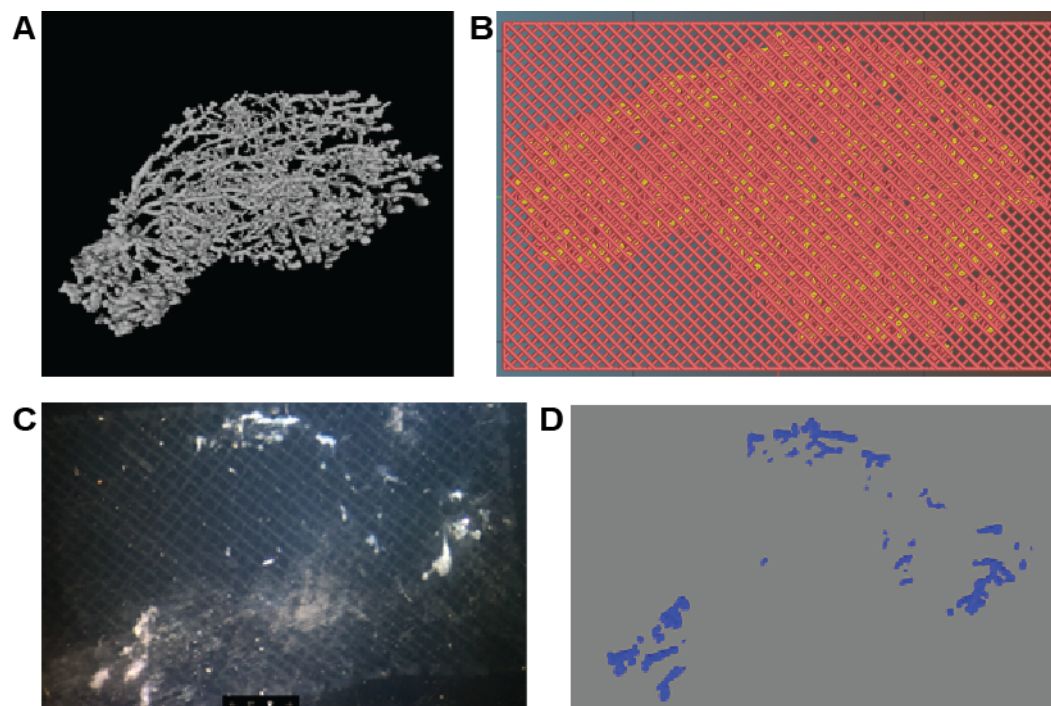


Figure 9. Producing Gcode for and troubleshooting a biomimetic mammary duct module. (A) A 6 wk. old KK/hlJ mammary duct is imaged and turned into this STL mesh representing the single largest connected surface which is, in turn, representative of the entire ductal tree. (B) Example Slic3r Gcode processing of (A), showing Collagen in yellow and alginate in red. (C) Printing the first 8 layers of the Gcode in (B) shows poor replication of collagen structures, which should appear like (D) The Gcode for the first 8 layers of collagen extrusion.

Executing the first few layers of the above Gcode using previously developed machine settings that worked best for simple constructs resulted in collagen extrusions shown in Figure 9C that did not resemble the Gcode portion sent to the printer (Figure 9D). The poor quality of collagen extrusion shown in Figure 9C was attributed to subtle vibrations of the extruder tips along the Z axis during movement in the XY plane. These vibrations were thought to be caused by the formation and disappearance of moments on the extruder during faster movements. To account

for this and other challenges presented by this print, it was decided to slow down the acceleration and instantaneous speed change settings to roughly half of their normal values. Additionally, the motors were provided with lower amounts of current to “smooth” out movements. Finally, the density of the alginate mesh support was increased from the 20% to 40%, providing much more support for collagen extrusions after release from the FRESH support bath.

Slower machine movements along with denser alginate mesh improved print quality substantially, resulting in the print shown in Figure 10A. This mammary duct model represents a world-first level of complexity generated using a bioprinter with multiple ECM and hydrogel components. This print takes approximately 2 hours to finish. Even at this slow rate, this print was printed faster than any commercial bioprinter could manage. A map of the printed construct generated using reflectance imaging tile scanning showed that features throughout the model were preserved in the output, shown below in Figure 10B and 10C. Distances measured between fiduciary regions of the file and print, shown highlighted with red stars in Figure 10B, indicated that the print underwent a roughly 4% shrinkage from its starting size. However, the shrinkage between fiduciary regions does not vary across at least one print. Repetition of these measurements are needed to confirm the maintenance of fidelity between file and print. Close-ups (Figure 10D) of the bottom left of the Gcode and the print’s reflectance image in Figure 10 show that there is apparent visual fidelity between the Gcode and the print at areas of high detail. This 3D printed structure will serve as a starting point for fabricating a complete model of duct development and cancer *in vitro*. The walls of a construct such as this are thin enough ($\leq 200\ \mu\text{m}$) that nutrient transport would not require vascularization. To fully utilize this model, many different support systems including perfusion culture and the endocrine effects of associated cell populations and stromal matrices would need to be incorporated. Even considering the challenges ahead, this model presents a complete solution to the mesoscale geometric complexity of branching epithelial networks.

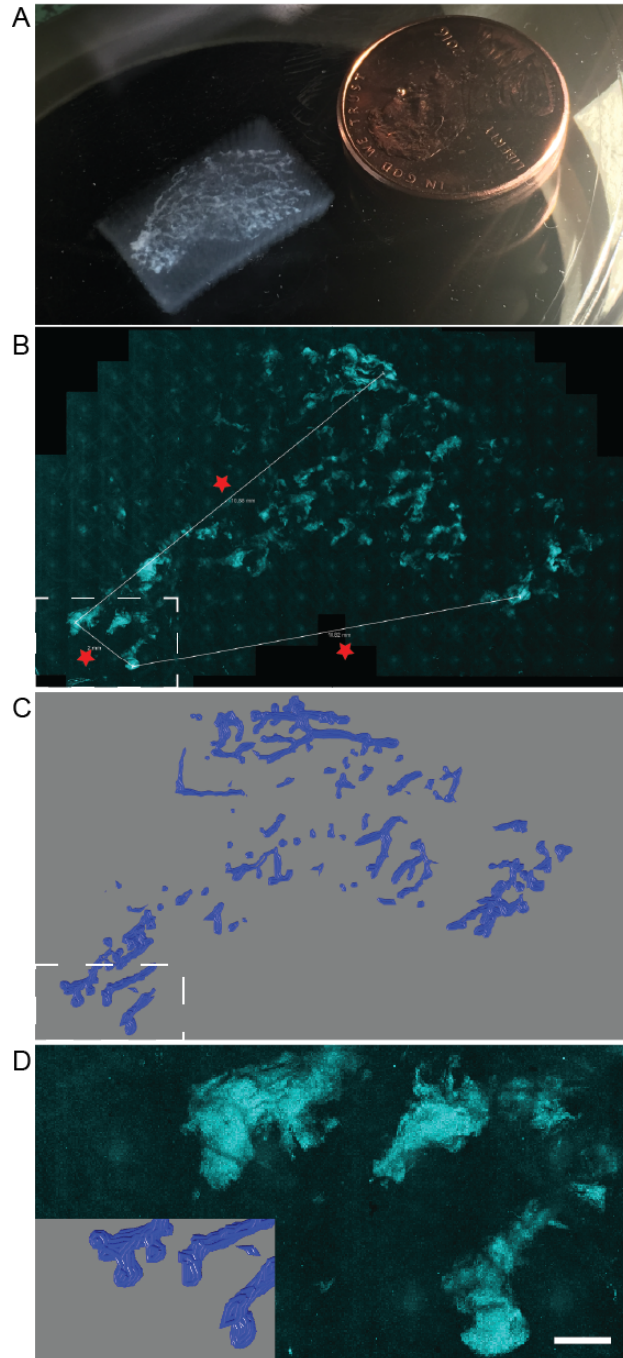


Figure 10. Biomimetic mammary duct print. (A) Shown submerged is the fully printed biomimetic collagen and alginate print of the file shown in Figure 4.8. The U.S. penny for scale shows that the print is faithful to the size of its file – 19 mm x 12 mm x 4 mm. (B) A max intensity projection of a reflectance tile scan shows that the print maintains fidelity in the first 12 layers of the print. The dashed box indicates an area shown in (D) Red stars indicate measured distances between fiduciary regions of the object. (C) Gcode of the first few layers of the print, showing the print maintains fidelity. Dashed box indicates area shown in (D) Close-up of the bottom left of (B & C) for comparison. Scale bar is 250 μ m.

Task 2 Subtask 3 was to be completed during months 8-12 and consisted of 3D printing the mammary ductal structure using progenitor cells (HMEC, MCF10A, HS578BSt). We have started this work and achieved the basic capability of seeding a simplified construct with mammary cells and evaluating adhesion, spreading and growth over time. Work is still on going to improve cell seeding and evaluate cell interaction.

To avoid the challenges of perfusion seeding and still enable distribution of cells throughout a construct with a sealed lumen, it was decided to try and seed constructs using a gravity-driven fluidic distribution system included in the mammary construct geometry. Mammary constructs had the same fundamental collagen component design of a funnel that fed into a tube “duct” which terminated in a spherical “bud”. It was assumed that the funnel could be held up above the surface of cell culture media and used as a receptacle for a cell suspension and allow cell suspension to flow down into the rest of the construct through the walls of the duct and bud. It was hypothesized that, were it not possible to seed the sides of the duct and bud using this approach, then the construct could be seeded in waves, and the construct could be rested on its side to allow for each wave of cells in to coat the sides of the duct and bud. To allow for introduction of the cell suspension to the funnel and for resting of the construct on its side, the alginate mesh reinforcement was designed as a cube centered on and surrounding the collagen component.

Part of the design process for the mammary constructs revolved around the capabilities of the 3D printing software and the printer. Since the smallest diameter needles we could utilize were 80 μm , we decided to design the collagen components to feature wall thicknesses in multiples of 80 μm . The interior lumen of the duct was the smallest feature of this print with an initial diameter of 200 μm in generation 1, but this value was increased to nearly 1 mm in generation 2. The resulting design features are shown in Figure 11. The size of the reinforcing alginate component was increased from 4 mm in X and Y to 8 mm to allow for easier handling of the entire construct.

For cell seeding post printing, constructs were thoroughly washed in warm 70 mM CaCl_2 with 25 mM Na-HEPES for at least 24 hours before submersion into 70 mM CaCl_2 with 25mM Na-HEPES and 50% v/v Ethanol. Constructs in this 50% Ethanol solution were then allowed to sit for 24 hours at 4°C. On the day of seeding and initiating culture, constructs were removed from this ethanol solution and placed into warm 70 mM CaCl_2 with 25mM Na-HEPES. After resting in this fluid for at least 30 minutes, the constructs were washed with fresh 70 mM CaCl_2 with 25mM Na-HEPES before being placed into cell media supplemented with 10 mM CaCl_2 .

ATCC MCF7 (HTB-22) and ATCC MCF 10A (CRL-10317) cells were transfected with pHIV-ZSGreen lentivirus and flow sorted to select for transfected cells. Resulting cells were cultured per ATCC guidelines. Constructs were washed in sterile-filtered 20°C 1% CaCl_2 with 25 mM Na-HEPES. Constructs were then soaked in 20°C sterile-filtered ATCC media, supplemented with 10 mM CaCl_2 and 200 $\mu\text{g/mL}$ Penicillin-Streptomycin for 10 minutes. Then constructs were placed in a 6-well plate with one construct per well. Supplemented media was added to each well until half of the construct was submerged (approximately 3 mL). Cells were suspended in supplemented media at 1×10^6 cells/mL. 50 μL of cells suspension was pipetted

directly into the center of the funnel portion of each construct. For half of the constructs, they were turned onto one of their 4 sides and allowed to rest there for 20 minutes at 37°C. Then, the seeding was repeated followed by 4 more resting periods until each construct was seeded on each side. Constructs were quickly imaged on an Olympus IX83 fluorescence microscope to ensure cells were in the constructs. One construct of the three for each cell type that was not rotated during seeding was seeded with 200,000 cells in the upright position. All constructs were finally returned to their upright conditions and placed in 37°C culture for 7 days, with regular media exchange. After 7 days, media was aspirated from each well before fixation.

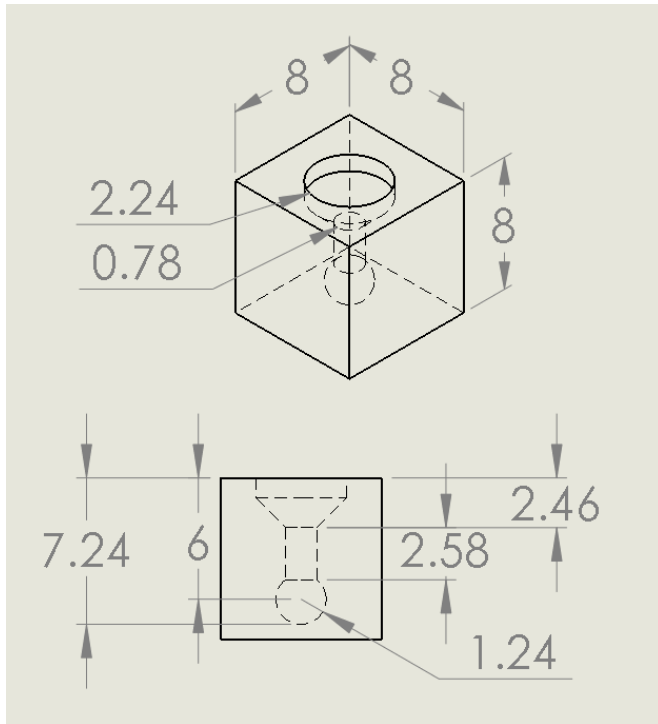


Figure 11. The CONSTRUCT parametric mammary duct module. The CONSTRUCT module features a vertical tube with a bulbous end and a funneled top. The dimensions of the construct were chosen based on what the printer was known to be capable of rendering in collagen type I.

Significant development effort was required to print these constructs. The most difficult aspect of this challenge was producing a wall of collagen material with uniform thickness across the entire length of the construct. After months of analysis, we determined that deflection of the small-diameter, 1 in long needle used as the extruder was the problem. During printing of the constructs for cell seeding, the needle was encountering the slurry's yield stress and was not able to exert a force large enough to overcome it until, like a spring, it developed a large enough internal strain – the deflection. Without physically altering the needle, it was thought that the Gcode instructions could be geometrically “hacked” to encourage the needle to more easily slide through the slurry. Typically, yield-stress fluids such as Bingham Plastics and Herschel-Bulkley models allow for the yield stress to dip if the fluid experiences a harmonic force. This effect is

attributable to physical vibrations interfering with the bonds associated with the yield stress of the material. For the regions of the construct that were the most prone to needle deflection, it was thought that a fine rectilinear raster pattern could be used to “jostle” the support and allow the needle to more easily progress. When this was applied to a couple of test prints, it was found to be unsuccessful in resolving closure of the duct. Therefore, it was necessary to physically reinforce the needle.

The 80 μm needle shown in Figure 12A was much stiffer after being reinforced (Figure 12B), and this allowed it to high-fidelity structures without closure of the duct (Figure 12C).

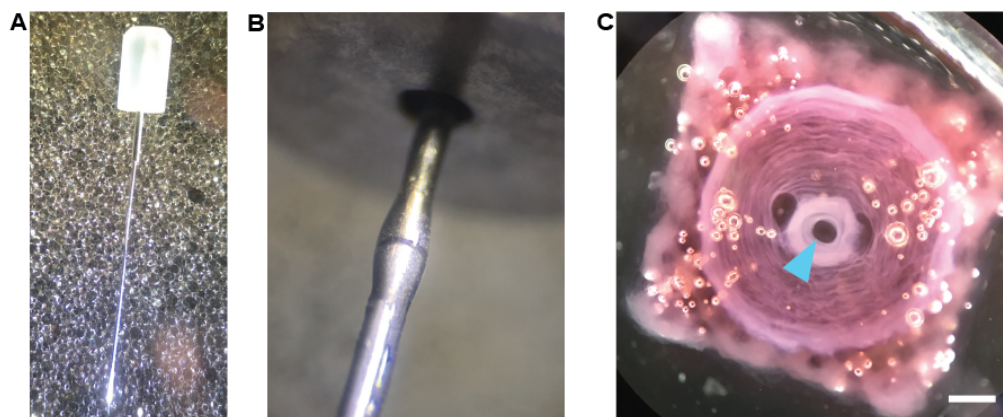


Figure 12. Physically reinforced needle produces better print outcome. (A) An un-reinforced 80 μm needle supplied by Hamilton for their GasTight® line of syringes with removable needle compression fittings. The glass ferrule is visible at the top, along with the slightly thicker section of metal just below the ferrule. The bottom of this needle is very flexible compared to standard luer-lock disposable deposition tips available from a large variety of suppliers. (B) A 250 μm needle removed from a luer fitting is slid over the 80 μm needle until it contacts the thicker metal near the glass ferrule in (A) and epoxied in place. Epoxy is visible as a bulge of clear material near the seam of the 80 μm needle (top) and the length of 250 μm needle (bottom) (C) The resulting print performed with a reinforced 80 μm needle shows an open duct when looking from above, and the overall diameter of collagen paths is larger due to the improved tracking of the 80 μm needle. Scale bar is 1 mm.

After the collagen extruder’s needle was reinforced, constructs created in a coacervate slurry possessed perfectly concentric circular extrusions of collagen, with little to no deflection or lagging of the extrusion visible. This quality of output is largely attributable to both the extra-fine texture of the coacervate, which has monodisperse, microscopic particles and the attention paid to alignment of separate extruder needles pre-print. The exterior of the constructs possessed a square profile with the 90° crosshatch pattern of alginate mesh. The rim of the funnel nearly always possessed a diameter within 1% of the intended value. Initial data shows that the internal diameter of the duct falls within approximately 2% of its intended value. The same data indicates that when the prints were released, post-culture, they were found to possess buds that

were always within 2% of the intended diameter of the file used to print them. Additional experimentation is still required to produce a statistically significant body of data.

Task 2 Subtask 4 was to be completed during months 10-14 and involved tomography imaging and evaluation of 3D progenitor cell-printed mammary ductal structure. A single sample will be evaluated. This work has been initiated as is ongoing. At this point we have developed the needed capabilities to image and analyze the printed, cellularized constructs and are currently collecting data.

Following culture Cultured CONSTRUCT's were rinsed with 1X PBS (supplemented with 0.625 mM $MgCl_2$ and 10 mM $CaCl_2$) at 37°C, fixed in 4% w/v formaldehyde with 10 mM $CaCl_2$ (Polysciences, Inc.) for 15 min, and then washed 3 times in 11 mM $CaCl_2$ with 25 mM Na-HEPES. The fixed CONSTRUCT was imaged with a Nikon AZ-C2 macro confocal microscope with a 5x objective (0.45 NA) and a Leica SP5 multiphoton microscope with a 10x (NA = 0.4) objective and a 25x (NA=0.95) water immersion objective. 3D image stacks were deconvolved with AutoQuant X3 and processed with Imaris 7.5.

In cases where the collagen and cells were obscured by alginate threads, it was possible to remove the alginate by washing a fixed construct in a 100 mM Na-Citrate buffer solution for 12 hours. Then, the construct could be embedded in 10% w/v Gelatin A and sectioned. The resulting collagen component with attached interior cells was then accessible by the microscopes. After removal of alginate threads, we acquired 3D z-stacks using reflectance imaging of collagen I at 435 nm with a Leica SP5 multiphoton microscope and a 25x water objective (NA = 0.95). Using ImageJ, we measured the thickness of the collagen I hydrogels in cross-section.

It wasn't known if the method of gravity seeding the constructs would result in the formation of a monolayer of cells on the inside surface of the collagen component. Fluorescent images of cells seeded into the constructs showed that cells did not always reach the duct and the end bud. It is thought that, occasionally, gelatin solution from the melting of the FRESH support bath does not entirely clear the duct and bud during post processing. In cases where gelatin may remain in the throat of the duct, it could prevent cell solution from entering the construct due to its viscosity. This blockage of cell suspension results in the seeded cells populating only the top portion of the duct and the funnel, as shown in Figure 13A. MCF7 cells expressing GFP are shown completely covering the surface of the funnel in Figure 13B.

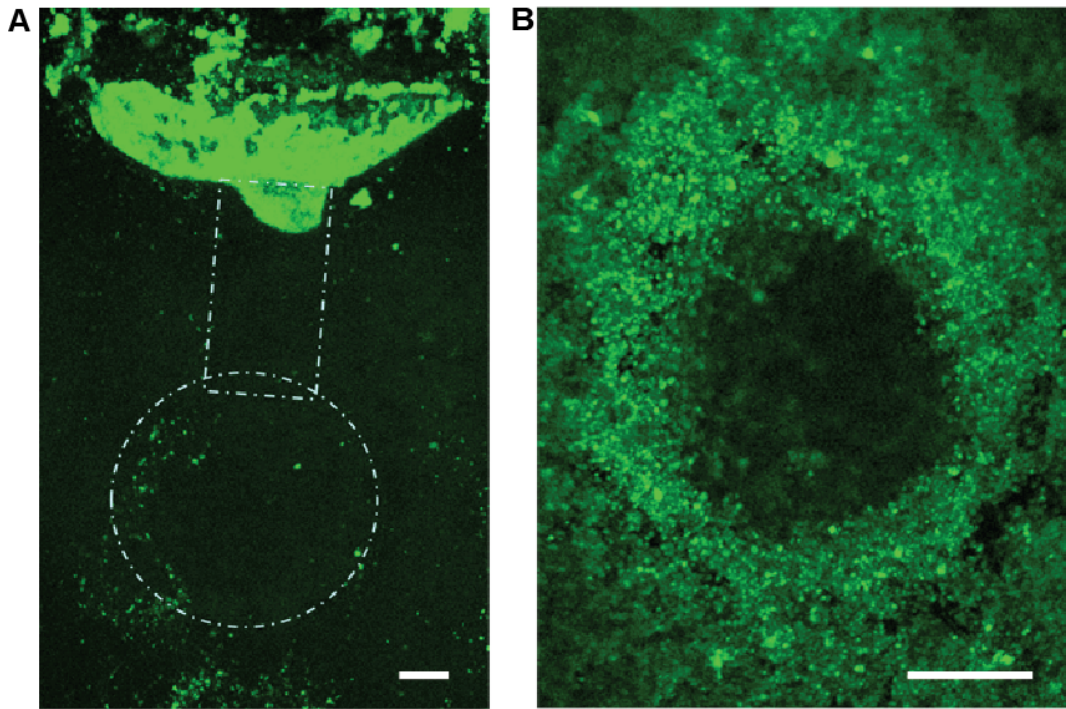


Figure 13. Seeding constructs can fail if the central tube of the construct is blocked with molten gelatin. (A) After a week of culture, MCF7 cells expressing GFP are shown to crowd the entrance to the CONSTRUCT construct, the rest of which is shown outlined in white dotted lines. It is thought that the cell suspension used to seed this construct could not enter the central tube and the terminal bud due to gelatin or excess hydrogel blocking the central tube. (B) A view from the top of the construct showing MCF7 cells adhered and growing in clusters around the entrance to the central tube. Scale bars are 1 mm.

In constructs seeded with MCF7 cells, fluorescence of cells was punctate and indicative of cells not covering the entire collagen surface inside the construct. Instead, cells grew in clusters, and the population of cells lining the duct and mouth of the funnel appeared rough, not possessing a smooth luminal surface, as seen in Figure 13B. In cultures of MCF10A cells, cell spreading on the constructs was much more pronounced, and cells formed a much smoother lumen shown in Figure 14.

The number of cells required to get adequate coverage of the collagen surfaces inside the construct was quite substantial – 50,000 cells per construct. MCF10A's expressing GFP were visibly covering the interior of the duct and bud, shown in Figure 14B and 14C. Gravity seeding constructs did not result in cells lining the top side of the bud, which is to be expected since settling cells will not have access to this portion of the construct. Interestingly, however, cells populated every other interior surface including the vertical walls of the duct tube. During culture, it may have been possible for cells to spread through defects to the outer surface, but no significant fluorescence was seen on collagen component exteriors. However, it is evident in Figure 14D that MCF10A cells are invading the collagen wall and are capable of smoothing the chaotic surface of the collagen which is slightly visible as a fuzzy cyan border on the left side of the image. In Figure 14E, the border between cells and collagen is clearly visible, but this was

not the case for the entire construct. A representative picture of epithelium on the interior surface, shown in Figure 14F, indicates that the cells form a smooth, multi-layered surface of cells regardless of the underlying collagen. Many iterations of seeding and construct design/print process were utilized to arrive at the current results. It is believed that the current seeding method will only benefit from higher cell numbers, and future plans include many replicates for the sake of obtaining statistically powerful insights on the nature of these rapidly prototyped tissues.

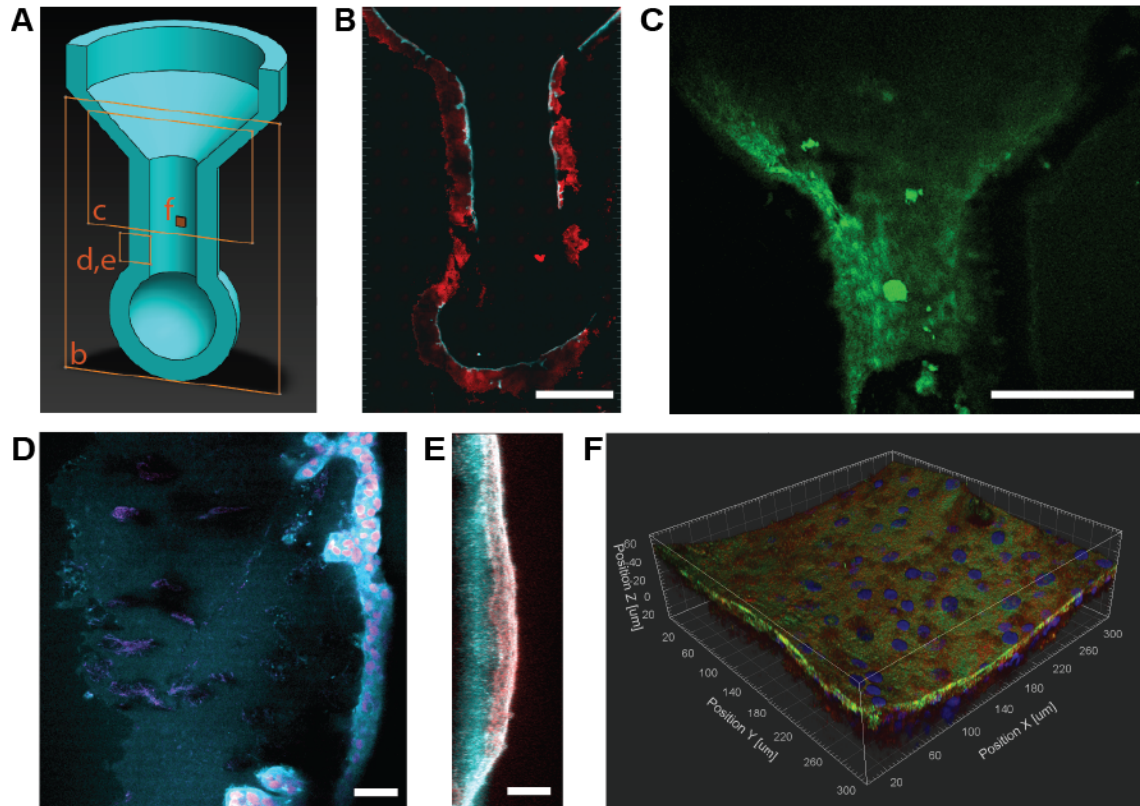


Figure 14. An epithelium of MCF10a cells coats the interior surface of a construct. (A) The CONSTRUCT shown with a cutaway to illustrate the regions imaged and shown in (B-F) (B) Collagen reflectance shown in red and GFP expression of MCF10a cells shown in cyan demonstrates the presence of a thin, continuous epithelium situated at the inside border of printed collagen hydrogel. (C) A max intensity projection of the construct shown in (A) which displays a coating of GFP-expressing MCF10A cells on the internal surface of the collagen. For (A) and (B) Scale bars are 1 mm. (D) Cyan actin (phalloidin) fluorescence with nuclei (DAPI) shown in magenta. The epithelium shows evidence of invading the collagen layers, as is shown by appendages of the epithelium extending from the luminal side (right) into the collagen. The exterior border of collagen is visible on the left of the image as a slight cyan fluorescence coming from overlap of the eosin fluorescence with actin fluorescence. Scale bar is 100 μm . (E) Another view of the epithelium showing cyan protein stain (eosin) and magenta actin (phalloidin) fluorescence with a clear boundary between cells and underlying collagen. Scale bar is 100 μm . (F) An isometric view of a z-stack of CONSTRUCT epithelium showing green actin (phalloidin), blue nuclei (DAPI), and red protein (eosin) fluorescence.

One concern regarding these constructs was whether the cells would compact the collagen component and cause a loss of structure. In all cases, constructs showed some degree of delamination between the alginate and collagen sections of the constructs visible at the rim of the funnel (Figure 15), regardless of cell type used. It is thought that this disconnection was the result of the collagen-alginate connection being particularly weak at the rim of the funnel. In future iterations of the construct, it would be straightforward to completely embed the rim of the construct into the surrounding alginate mesh fibers, thereby preventing it from disconnecting. To investigate the effects of cells on the interior dimensions of the collagen component, it will be necessary to repeat these experiments and utilize a tomographic imaging approach to resolve internal architecture.

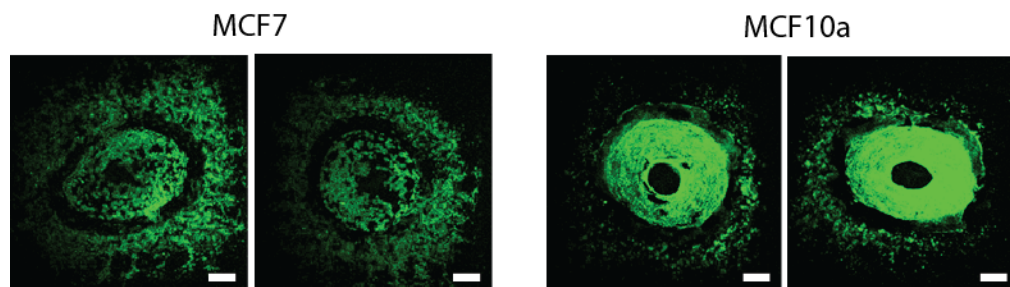


Figure 15. Delamination of collagen is consistent across constructs seeded and cultured for a week. Constructs shown on the left were cultured with MCF7 cells, and constructs on the right were cultured with MCF10a cells. In all constructs, a gap of cells was visible around the top rim of collagen, indicating that the collagen was originally there but pulled away under the action of cells. Otherwise, we would expect to see cells scattered around the edge of the rim on all regions of top-side alginate. Scale bars are 1 mm.

4) Impact

Our data thus far indicate that different strains of mice exhibit different mammary gland structures, suggesting a genetic component to development. Having a comprehensive quantification of mammary gland development may yield insight into risk factors for subsequent development of breast cancer.

3D printing of mammary glands is progressing. 3D printing of a simplified tube was successful and we were able to place breast cancer cells in the tube, placing us on the path to successfully mimicking DCIS in vitro. We also demonstrated the ability to print an entire mammary duct network based on 3D OPT imaging data. If successful this model will provide unique biologic insight into breast cancer progression.

5) Changes/problems

There are no major challenges/problems that require a major change to the overall proposal. We have encountered numerous minor difficulties such as reduced fecundity in some mouse strains, issues with wavelength choice and availability on microscopes etc. However we believe we are able to overcome most of these challenges.

6) Products

Whole mounts of murine mammary glands

Images and reconstructions of mammary glands

3D printed tubes representing ducts

7) Participants and other collaborating organizations

Darryl Hadsell PhD, Baylor College of Medicine (subcontract)

Adrian Lee, PhD, University of Pittsburgh (Partnering PI)

Adam Feinberg, PhD, Carnegie Mellon University (Partnering PI)

Priscilla McAuliffe MD, PhD University of Pittsburgh (Co-Investigator)

8) Special reporting requirements

None

9) Appendices

None